Volume 54
Number 36
28 September 2025
Pages 13367-13792

Dalton Transactions

An international journal of inorganic chemistry

rsc.li/dalton

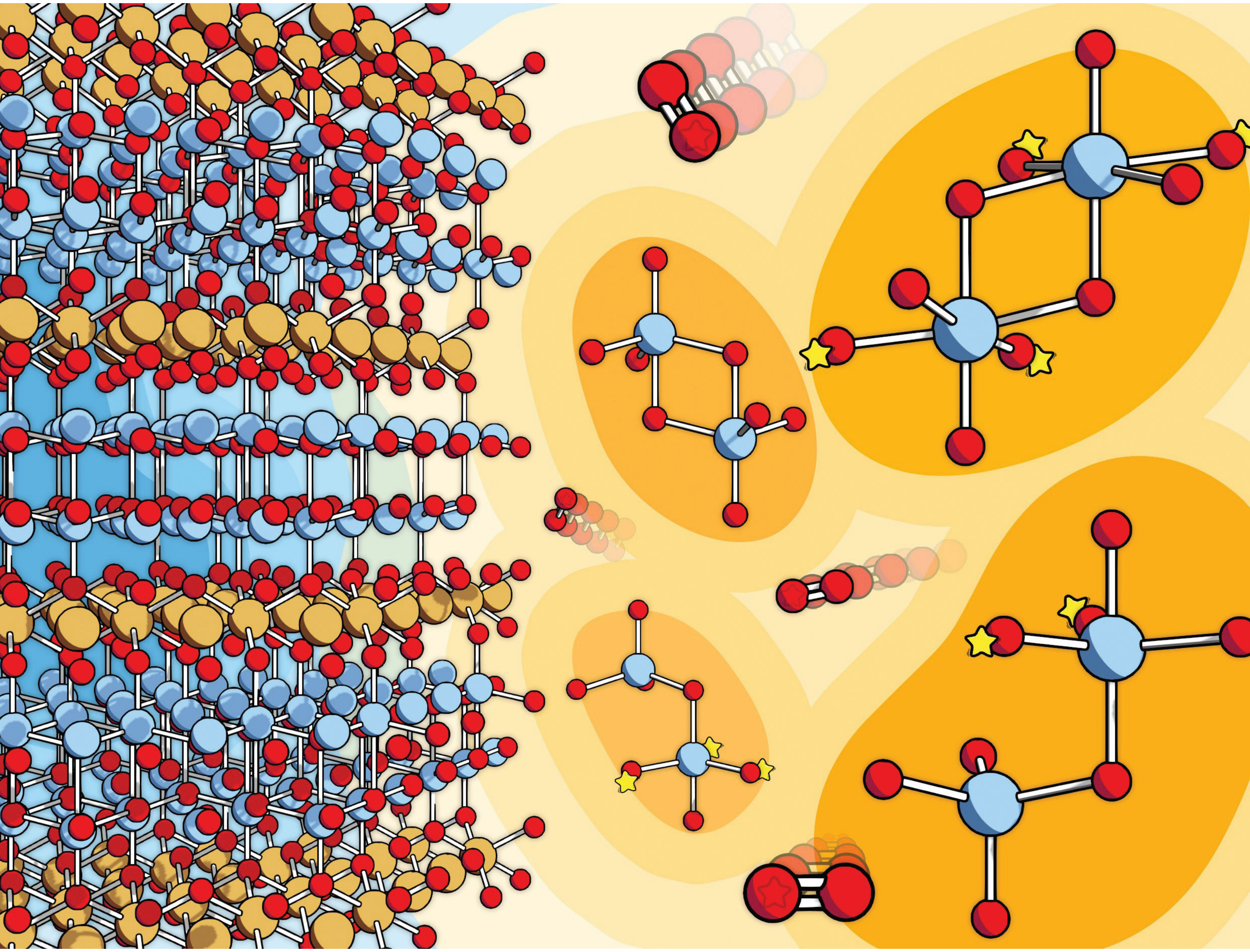

ISSN 1477-9226

ROYAL SOCIETY
OF **CHEMISTRY**

PAPER
Efrain E. Rodriguez *et al.*
Reversible structural and colorimetric transitions in $LuMnGaO_4$ upon oxygen uptake and release

Dalton Transactions

ROYAL SOCIETY OF CHEMISTRY

PAPER

View Article Online
View Journal | View Issue

Check for updates

Cite this: *Dalton Trans.*, 2025, **54**, 13431

Reversible structural and colorimetric transitions in $LuMnGaO_4$ upon oxygen uptake and release†

Stephanie J. Hong, ‡[a] Tianyu Li, ‡[a,b] H. Cein Mandujano,[a] Alicia Manjón-Sanz,[c] Sz-Chian Liou,[d] Yuchen Niu[a] and Efrain E. Rodriguez *[a]

Received 2nd April 2025,
Accepted 1st July 2025

DOI: 10.1039/d5dt00798d

rsc.li/dalton

We synthesized $LuMnGaO_4$, an AB_2O_4-type compound, and performed structural analysis and characterization focusing on its reversible oxygen uptake and oxidation-driven color change. The reduced phase, $LuMnGaO_4$, synthesized *via* solid-state reactions, crystallizes in the $R\bar{3}m$ space group. Heating this metal oxide in an oxygen-rich environment induces a phase transition to the oxidized phase, $LuMnGaO_{4.5}$, which adopts the $P\bar{3}$ space group. Through neutron diffraction studies, we elucidate the structural transition upon oxygen uptake, while *in situ* synchrotron X-ray powder diffraction confirms a low temperature ($\sim T$ = 250 °C) transition. The oxidation process induces a significant color shift from greenish-grey to black, and we quantify this electronic transition by UV-visible spectroscopy. Electron diffraction and synchrotron X-ray data further reveal structural modulations in the form of superlattice reflections and diffuse scattering associated with oxygen disorder in the oxidized phase. The diffraction data show that the reversible oxygen uptake and release occurs in the bulk phase at relatively low temperatures, suggesting applications in oxygen transport technologies. Furthermore, the distinct color change highlights its potential as a bifunctional material for oxygen carriers and colorimetric oxygen sensors. This work provides a foundation for future exploration of the structural and electronic evolution of AB_2O_4-type compounds during oxygen uptake and release.

1. Introduction

Transition metal oxides capable of reversibly taking up and releasing oxygen are crucial for a wide range of technological applications.[1–5] These materials have been extensively studied as oxygen carriers or transport materials in chemical-looping technologies, such as combustion, reforming, and gasification.[6,7] These processes involve redox cycles where the oxides are reduced by fuels and reoxidized in air.

Metal oxides are also increasingly explored in chemical-looping water splitting and solar thermal water splitting for sustainable hydrogen production and energy storage.[8] Non-stoichiometric perovskite oxides, such as $Sr_xLa_{1-x}Mn_yAl_{1-y}O_{3-\delta}$[9] and $BaCe_xMn_{1-x}O_3$ (BCM),[10] have been widely studied for these applications. However, their high oxidation/reduction temperatures pose a significant challenge, limiting their practical applicability.[11,12] Developing materials that can undergo redox cycles at lower temperatures is essential to improve energy efficiency and broaden their usability.

Recent advancements have broadened the scope of oxygen carrier materials beyond traditional binary metal oxides and perovskite-related oxides to include hexagonal layered $AB^{2+}B^{3+}O_4$-type compounds (A = rare earth metals; B = transitional metals).[11–15] These materials, characterized by a trigonal structure of alternating octahedrally coordinated rare earth metal layers and transition metal double bipyramidal layers, were initially recognized for their multiferroic properties.[16] $LuFe_2O_4$ was the first $AB^{2+}B^{3+}O_4$ compound reported to reversibly uptake oxygen at 200 °C, which is a relatively low temperature compared to previously known oxides, forming $LuFe_2O_{4+x}$ and reverting to its reduced phase.[16,17] Following this discovery, various A-site and B-site substituted compounds demonstrated similar oxygen storage capacities at temperatures around 250–300 °C in our previous work.[18–21] In $LuMnFeO_4$, redox-active Mn^{2+} was substituted for Fe^{2+}, while Fe^{3+} occupied the redox-inactive site. This compound exhibited similar redox behavior to $LuFe_2O_4$, undergoing a phase transition from $R\bar{3}m$ to $P\bar{3}$ symmetry during oxygen absorption, forming $LuMnFeO_{4.5}$.[21] To further investigate the effects of B-site substitution on structure and redox behavior, we substituted Ga^{3+} for Fe^{3+} to form $LuMnGaO_4$. The greater disparity in size and chemical properties between Mn and Ga, compared to Mn and

---

[a] *Department of Chemistry and Biochemistry, University of Maryland, College Park, Maryland 20742, USA. E-mail: efrain@umd.edu*
[b] *Materials Research Laboratory, University of California, Santa Barbara, California 93106, USA*
[c] *Neutron Scattering Division, Oak Ridge National Laboratory, Oak Ridge, Tennessee 37831, USA*
[d] *Institute for Functional Materials and Devices, Lehigh University, Bethlehem, Pennsylvania 18015, USA*

† Electronic supplementary information (ESI) available. See DOI: **https://doi.org/10.1039/d5dt00798d**

‡ Equal contribution.

Fe provided an opportunity to investigate the impact of elemental substitution on structural and redox characteristics.

In addition to oxygen storage, oxygen sensors play a critical role in modern technologies, with applications spanning food production, automotive systems, healthcare, and environmental monitoring.[22–24] These sensors, categorized by mechanisms such as electrochemical, resistive, and optical methods, are designed to monitor oxygen levels accurately.[25–27] Developing materials that not only store oxygen but also enable real-time sensing of oxygen capacity offers exciting opportunities for advancing sensor technologies. Such multifunctional materials could revolutionize oxygen monitoring by integrating storage and sensing capabilities into a single platform.

In this study, we present a comprehensive investigation of $LuMnGaO_4$ and its oxidized phase, utilizing neutron and synchrotron X-ray powder diffraction (SXPD). *In situ* SXPD revealed phase transitions and structural modulations in the oxidized phase. Notably, $LuMnGaO_4$ displayed a color change from greenish-grey to black upon oxidation, a phenomenon not observed in previously studied $LnFe_2O_4$ and $LnMnFeO_4$ compounds. We establish a correlation between this color transition and the changes in the oxygen environment surrounding Mn due to structural evolution during oxidation. This distinct color change suggests potential applications for $LuMnGaO_4$ not only in oxygen transport but also in oxygen sensing, highlighting its potential as a bifunctional material.

2. Method

2.1 Materials synthesis

The reduced phase, $LuMnGaO_4$, was synthesized *via* solid-state reactions.[13] Stoichiometric amounts of Lu_2O_3 (99.999%), MnO (99%), and Ga_2O_3 (99.999%) were ground to produce 2 g of the target compound. The powder mixture was pressed into 13 mm diameter pellets, placed in a 2 mL alumina crucible, and sealed inside an evacuated 8 mm diameter quartz ampoule. The ampoule was heated to 1180 °C at a ramp rate of 5 °C min^{-1}, held at this temperature for 24 hours, and then rapidly quenched in an ice-water bath to preserve the metastable $LuMnGaO_4$ phase and prevent the formation of oxide impurities. The oxidized phase, $LuMnGaO_{4.5}$, was prepared by heating $LuMnGaO_4$ at 600 °C in ambient air for 12 hours, followed by a natural cooling to room temperature.

2.2 Thermogravimetric analysis (TGA)

TGA was conducted on the reduced phase, $LuMnGaO_4$, using a Mettler Toledo TGA/DSC 2 HT 1600. Approximately 5 mg of the sample was heated in air to 700 °C with a ramp rate of 10 °C min^{-1}. For reduction studies, 10 mg of the oxidized phase was heated to 800 °C in 3% H_2/Ar.

2.3 X-ray photoelectron spectroscopy (XPS)

XPS data were collected using a Kratos AXIS Supra + X-ray photoelectron spectrometer equipped with a monochromatic Al Kα X-ray source (1486.6 eV, 225 W). The base pressure of the analysis chamber was $\sim 1 \times 10^{-9}$ torr. Spectra were acquired in hybrid lens mode with slot collimation and a spot size of 700 μm × 300 μm. The pass energy and step sizes were set to 160 eV and 0.5 eV for survey spectra, and 20 eV and 0.1 eV for high-resolution spectra, respectively. Samples were grounded during analysis, and charging effects were minimized using a charge neutralizer. Instrument calibration was performed using Au $4f_{7/2}$ (84.0 eV) and Cu $2p_{3/2}$ (932.6 eV) peaks from sputter-cleaned metal foils.

Data calibration involved aligning the adventitious C 1s peak to 284.8 eV. Deconvolution was performed using a Voigt peak profile (70% Gaussian, 30% Lorentzian) after Shirley background subtraction. For Ga and Lu quantification, the Ga $3p_{3/2}$ and Lu $4p_{3/2}$ peaks were used, with sensitivity factors adjusted based on spin–orbit splitting ratios of p orbitals. All data were analyzed using CasaXPS software.[28]

2.4 Electron paramagnetic resonance (EPR)

EPR measurements were carried out using a Bruker EMXPlus X-band spectrometer equipped with a high-sensitivity Bruker ER 4199HS-LC resonator. Spectral acquisition involved averaging three scans over a field sweep of 0 mT to 600 mT, with a magnetic field modulation of 100 kHz and a modulation amplitude of 0.4 mT. Data processing and spectral fitting were performed using the EasySpin toolbox.[29] Standard (non-*operando*) measurements were conducted at a microwave power of 2 mW.

2.5 High-resolution synchrotron X-ray and neutron diffraction

High-resolution synchrotron X-ray powder diffraction (SXPD) was performed to characterize the crystal structures of $LuMnGaO_4$ and $LuMnGaO_{4.5}$. Measurements were conducted at the Advanced Photon Source (APS), Argonne National Laboratory, on the 11-BM beamline using X-rays with a wavelength of 0.457895 Å. Data were collected at room temperature (300 K). Time-of-flight (TOF) neutron diffraction experiments were conducted on the POWGEN[30] beamline at the Spallation Neutron Source, Oak Ridge National Laboratory, with data acquired at 300 K. Structural analysis was performed using Rietveld refinement with the GSAS-II software.[31]

For *in situ* SXPD studies, data were collected on the APS 11-ID-C beamline using a high-temperature furnace. A wavelength of 0.1173 Å was used, covering a *Q*-range of ~0.6 $Å^{-1}$ to 11 $Å^{-1}$. The sample was heated at a controlled ramp rate of 10 °C min^{-1} in flowing air, diffraction patterns continuously recorded during heating to monitor the real-time structural evolution of $LuMnGaO_4$.

2.6 Raman spectroscopy

Raman spectra were collected from powder samples using a HORIBA Yvon Jobin LabRam ARAMIS Raman microscope, equipped with a 400 μm pinhole, 100 μm slit, a 50× objective (NA = 0.9), and a 532 nm laser delivering 21 mW of power at the sample. To minimize laser absorption and prevent sample oxidation, a D2 filter and an extended exposure time (>5 min) were employed to improve the Raman scattering signal.

2.7 Transmission electron microscopy (TEM)

Transmission electron microscopy (TEM) and selected area electron diffraction (SAED) patterns were acquired using a JEOL 2100F field emission gun (scanning) TEM [FEG-(S)TEM] and operated at an accelerating voltage of 200 kV.

2.8 UV-vis reflectance spectroscopy

Diffuse reflectance spectra of the powder samples were obtained using a Shimadzu UV3600 UV-vis-NIR spectrometer equipped with an integrating sphere attachment. Prior to measurement, the powders were diluted with BaSO4 in a 1 : 4 volume ratio and packed into solid sample holders. The recorded reflectance spectra were processed into pseudo-absorbance using the Kubelka–Munk transformation.

2.9 Energy dispersive X-ray spectroscopy (EDS)

The chemical composition of the reduced and oxidized phases was analyzed on powder samples using Hitachi SU-70 Schottky FEG-SEM equipped with the Bruker energy dispersive X-ray spectroscopy (EDS, XFlash(6/60)). The analysis results are in Table S9.†

3. Results and discussion

3.1 Reversible oxygen uptake of $LuMnGaO_4$

Previous studies have demonstrated that $LnFe_2O_4$[16,19] and $LnFeMnO_4$[21] (Ln = lanthanides) compounds can uptake oxygen at elevated temperatures, leading to the oxidation of Fe^{2+} to Fe^{3+} ($LnFe_2O_4$) or Mn^{2+} to Mn^{3+} ($LnFeMnO_4$) and the formation of final products $LnFe_2O_{4.5}$ and $LnFeMnO_{4.5}$. Similarly, we examined the oxygen uptake behavior of $LuMnGaO_4$, which contains the redox-active element Mn^{2+} and shares structural similarities with $LnFe_2O_4$[16,19] and $LnFeMnO_4$.[21] Thermogravimetric analysis (TGA) was performed on $LuMnGaO_4$ under flowing air. As shown in Fig. 1a and Fig. S9,† $LuMnGaO_4$ begins to absorb oxygen at approximately 250 °C, a higher temperature than $LnFe_2O_4$ (<200 °C)[16] and $LnFeMnO_4$ (~200 °C).[21] The oxidation process results in a

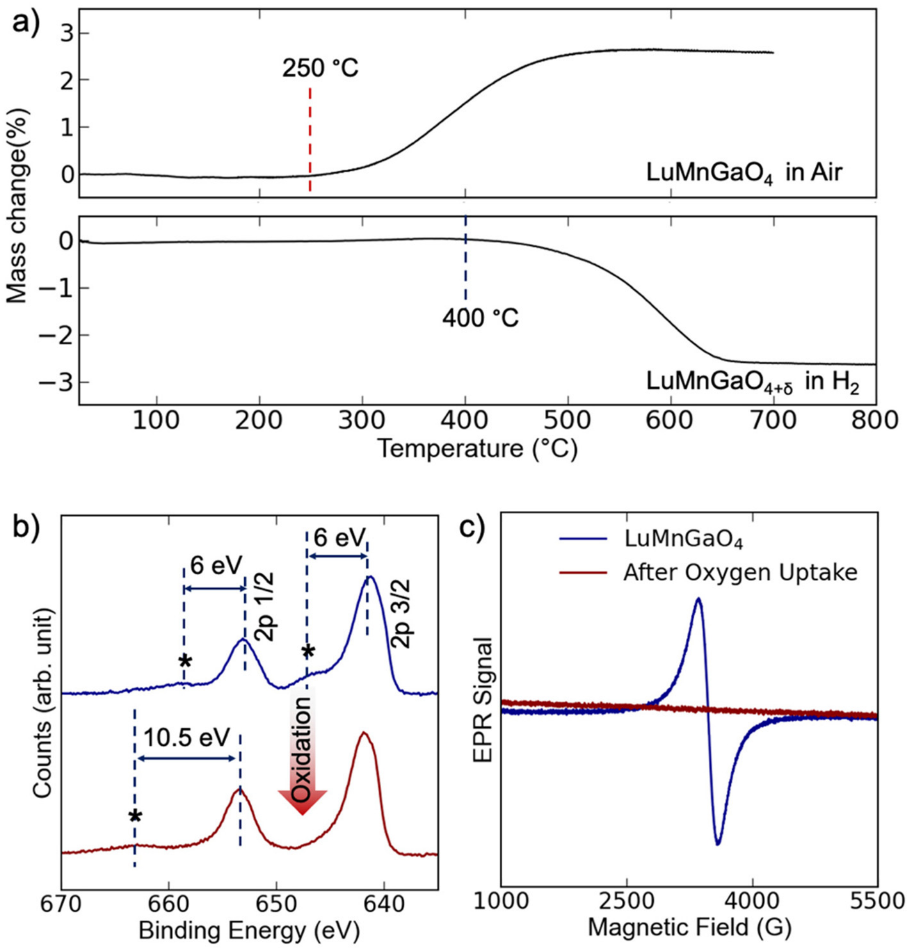

Fig. 1 (a) Thermogravimetric analysis (TGA) measurements for $LuMnGaO_4$ in air (top) and $LuMnGaO_{4.5}$ in 3% H_2/Ar atmosphere (bottom). (b) Mn 2p XPS spectra comparison between $LuMnGaO_4$ and $LuMnGaO_{4.5}$. (c) EPR Spectra of the samples.

2.57(1) % weight gain in the final product, corresponding to an uptake of 0.603(2) oxygen atoms per formula unit. This value slightly exceeds the 0.5 moles of oxygen atoms expected from full oxidation of Mn^{2+} to Mn^{3+}. We attribute this to slight oxygen deficiency in the starting reduced material ($LuMnGaO_{4-\delta}$), which would result in a slightly greater weight gain upon oxidation.

To further verify the valence change of $LuMnGaO_4$ upon oxidation, XPS and EPR measurements were conducted on $LuMnGaO_4$ before and after oxidation. The Mn 2p XPS spectra are shown in Fig. 1b. For $LuMnGaO_4$, the binding energy of Mn $2p_{3/2}$ and the satellite separation are 641.2 eV and 5.6 eV, respectively, while for $LuMnGaO_{4.5}$, these values are 641.8 eV and 10.5 eV. These results are consistent with reported values for Mn^{2+} and Mn^{3+} in MnO and Mn_2O_3.[32–35] Additional analysis on Mn 3s XPS spectra is included in the ESI (Fig. S1).†

EPR measurements further corroborated the oxidation from Mn^{2+} to Mn^{3+}. Since Mn is the only magnetic center in $LuMnGaO_{4+x}$, the EPR signal of $LuMnGaO_{4+x}$ exclusively originates from Mn. In parallel-mode X-band EPR spectroscopy, only ions with non-integer spin values respond to the magnetic field gradient.[36] The Mn^{2+} cations in $LuMnGaO_4$ are S = 5/2 (d^5, high spin) or S = 3/2 from 3 e^- occupation of the e″ manifold and, therefore, displays an EPR response, as presented in Fig. 1c. However, after oxygen uptake, the EPR signal becomes silent, indicating oxidation to Mn^{3+} (d^4, S = 2) rather than Mn^{4+} (d^3, S = 3/2).

Overall, the TGA, XPS, and EPR data consistently demonstrate that $LuMnGaO_4$ transforms into $LuMnGaO_{4.5}$ upon oxygen uptake, accompanied by the oxidation of Mn^{2+} to Mn^{3+} within the structure. To investigate the reversibility of this process, TGA measurements were performed on the oxidized phase, $LuMnGaO_{4.5}$, under a reducing atmosphere (3% H_2/Ar gas), as shown in Fig. 1a. A weight decrease of −2.64(1) % was observed in the final product, indicating a reversible oxygen release, converting $LuMnGaO_{4.5}$ back to $LuMnGaO_4$. After reduction, the sample returned to its original greenish-grey color.

3.2 Crystal structure of the reduced phase $LuMnGaO_4$

The room-temperature neutron diffraction pattern of $LuMnGaO_4$, along with its Rietveld refinement, is shown in Fig. 2a. The structure was confirmed to be isostructural to the parent phase $LnFe_2O_4$,[11,12,37] belonging to space group $R\bar{3}m$, which served as the initial model for the refinement. The phase is nearly pure, with a minimal impurity of $Lu_3Ga_5O_{12}$ (<0.3%). The structure consists of alternating layers of Lu in octahedral coordination layers and trigonal bipyramidal Mn/Ga, where Mn and Ga are completely disordered as illustrated in Fig. 3a.[12,38]

The refinement was initially conducted with Lu positioned at the Wyckoff position, 3a (0, 0, 0), yielding an agreement index (R_{wp}) value of 8.198% (Fig. S4, Table S2†). The subsequent introduction of anisotropic thermal displacement for Lu reduced the R_{wp} by half (Fig. S5, Table S3†). However, the notable large thermal parameter along the c-axis for Lu indicated static disorder in its positional arrangement along this direction, a phenomenon commonly observed in related compounds.[20,39] Consequently, in the final structural model, Lu was slightly displaced from its ideal position and assigned to the 6c (0, 0, z) site,[40] with the refined value of z = 0.00675(4). In this final refinement, the thermal vibration for Lu was isotropically refined, yielding a satisfactory fit consistent with previous observations for $LuCuGaO_4$.[40] The refinement parameters are summarized in Table 1. The positional disorder of Lu is likely due to the significant chemical disparity between Mn and Ga, which share the same crystallographic site. The size difference between Mn (0.75 Å)[41] and Ga (0.55 Å)[41] creates variations in the local environment, particularly in their interactions with surrounding oxygen atoms bonded to Lu, resulting in a displacement of Lu along the c-axis.

The crystal structure of hexagonal-type AB_2O_4 compounds can also be represented by the space group $C2/m$, a maximal non-isomorphic subgroup of $R\bar{3}m$.[42] The Rietveld refinement of the neutron pattern is shown in Fig. S2.† Refinement of the anisotropic thermal vibration of Lu and oxygen atoms yielded an R_{wp} of 4.793%, with a notably large thermal elongation of Lu along the c-axis, similar to the case for $R\bar{3}m$ (Tables S1 and S3†). However, no peak splitting due to lattice distortion was observed in the Bragg peaks of the neutron diffraction pattern or high-resolution SXPD patterns (Fig. S2 and S3†), indicating no need to lower the symmetry. Therefore, we conclude that the space group $R\bar{3}m$ best describes the reduced phase, $LuMnGaO_4$.

3.3 Crystal structure of the oxidized phase, $LuMnGaO_{4.5}$

As anticipated from similar compounds, $LuMnGaO_{4.5}$ is structurally distinct compared to its reduced phase, $LuMnGaO_4$.[19–21] A significant change in diffraction patterns (X-ray and neutron) is observed upon the oxygen uptake of $LuMnGaO_4$ (Fig. 2b and Fig. S11†). The Raman modes also show notable deviations before and after oxidation, indicating a change in crystal symmetry (Fig. S17†). Previous studies suggest that $LnFe_2O_4$ and $LnFeMnO_4$ transition from the $R\bar{3}m$ to $P\bar{3}$ space group upon oxidation.[16–19,43] Here, the $P\bar{3}$ structural model of $LnFe_2O_{4.5}$ and $LnFeMnO_{4.5}$ was used as the starting model to refine the average structure of $LuMnGaO_{4.5}$, yielding good agreement with the observed diffraction pattern, as shown in Fig. 2b.

Initial refinements were conducted with Lu maintained at its special position (0, 0, 0) and isotropic thermal parameters, resulting in an R_{wp} value of 8.576% (Fig. S6 and Table S4†). Subsequent refinement of the thermal parameters for Lu and the oxygen atoms improved the fit. Similar to the refinement of $LuMnGaO_4$, Lu exhibited an unusual ellipsoidal elongation along the c-axis. Therefore, Lu was assigned to the 2c (0, 0, z) site, slightly shifted from its ideal position. The O2 and O3 oxygen atoms also exhibited elongation in the xy-plane, leading to slight shifts that placed them in disordered positions (Fig. S7 and Table S5†). This oxygen disorder was identified for the first time in $LnM_2O_{4.5}$-type materials and attributed to the distinct chemical and size disparity between Mn and Ga. Compared to compounds where B sites are occupied by

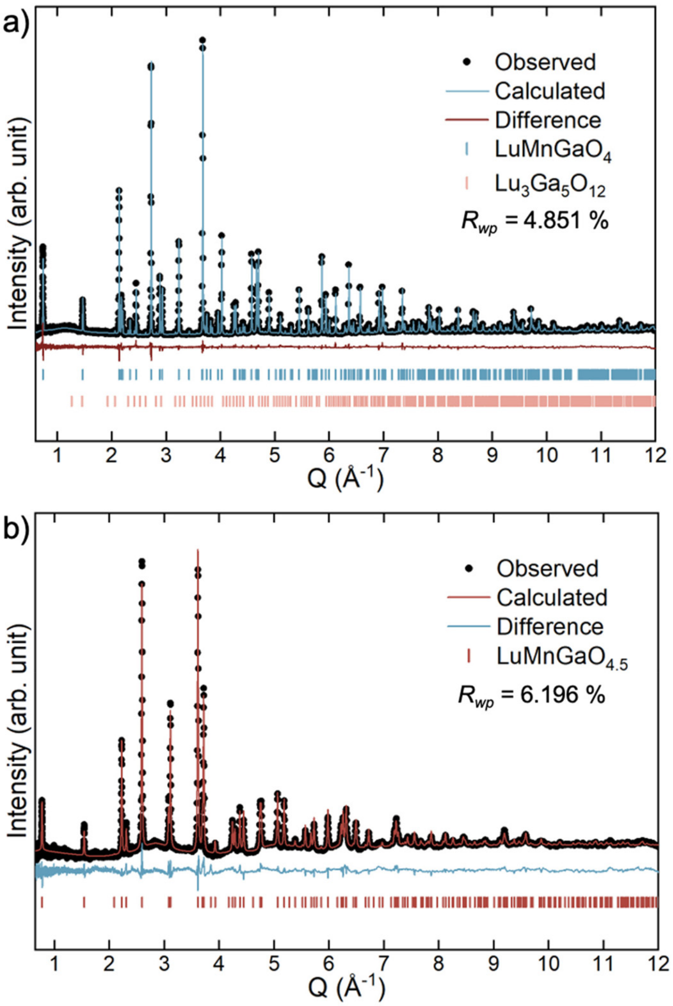

Fig. 2 Neutron powder diffraction patterns with Rietveld fits for (a) the reduced phase, $LuMnGaO_4$, and (b) the oxidized phase, $LuMnGaO_{4.5}$. Data were collected using the POWGEN[30] instrument at the Spallation Neutron Source, Oak Ridge National Laboratory, with a center wavelength of 0.8 Å at 300 K.

similar ions (*e.g.*, Fe^{2+}/Fe^{3+}or Mn^{2+}/Fe^{3+}),[20,21] the significant differences between Mn^{2+} and Ga^{3+} ionic radii contribute to local disorder. This disparity is evident when comparing neutron and electron diffraction patterns, as materials with less ion size disparity exhibit substantially less diffuse scattering than $LuMnGaO_{4.5}$.[20,21,42] Additionally, this oxygen disorder brought on by Mn/Ga mixing leads to a more diffuse nature in the superlattice reflections, which get broadened out into the background of the neutron (Fig. 2b) and 11-BM powder diffraction patterns (Fig. S11†). For the final refinement, the occupancies of O2 and O3 oxygens were constrained to have a sum of 0.417, and only the isotropic thermFal parameters were refined. The final refinement results are provided in Table 2. The results from a dual refinement of the oxidized phase's structure at 300 K with both the neutron diffraction and synchrotron PXRD data sets can be found in Fig. S12† and the resulting structural parameters in Table S8.†

As shown in Fig. 3b, oxygen is inserted into the Mn/Ga–O layers to occupy the O3 sites. The disordered oxygen sites are depicted in Fig. 3c. The Mn/Ga site in the bilayer is coordinated by eight oxygen atoms, with partial occupancy at the O2 and O3 positions, which cannot be occupied simultaneously due to their short interatomic distance of 1.589(7) Å. This suggests that the observed Mn/Ga–O_n polyhedral structure represents the average of multiple local polyhedral configurations. In a previous study on $YbFe_2O_{4.5}$, Nicoud *et al.* described a rearrangement of Fe coordination polyhedra following the insertion of interstitial oxygen, forming a range of FeO_n polyhedral units (n = 4, 5, 6) within the double bipyramid layer.[20] Similarly, for $LuMnGaO_{4.5}$, we propose that the bilayer consists of a superimposition of trigonal bipyramid, tetrahedral, and octahedral polyhedra (Fig. 3d). Ours is a qualitative suggestion based on the work by Nicoud *et al.*,[20] as we have not conducted a quantitative analysis to determine the exact proportion of each polyhedral unit. The splitting of oxygen positions O2 and O3 from their special positions indicates complex oxygen disorder, likely contributing to the structural modulation observed in the oxidized phase, as evident in the selected-area electron diffraction (SAED) patterns discussed below (Fig. 4d–f).

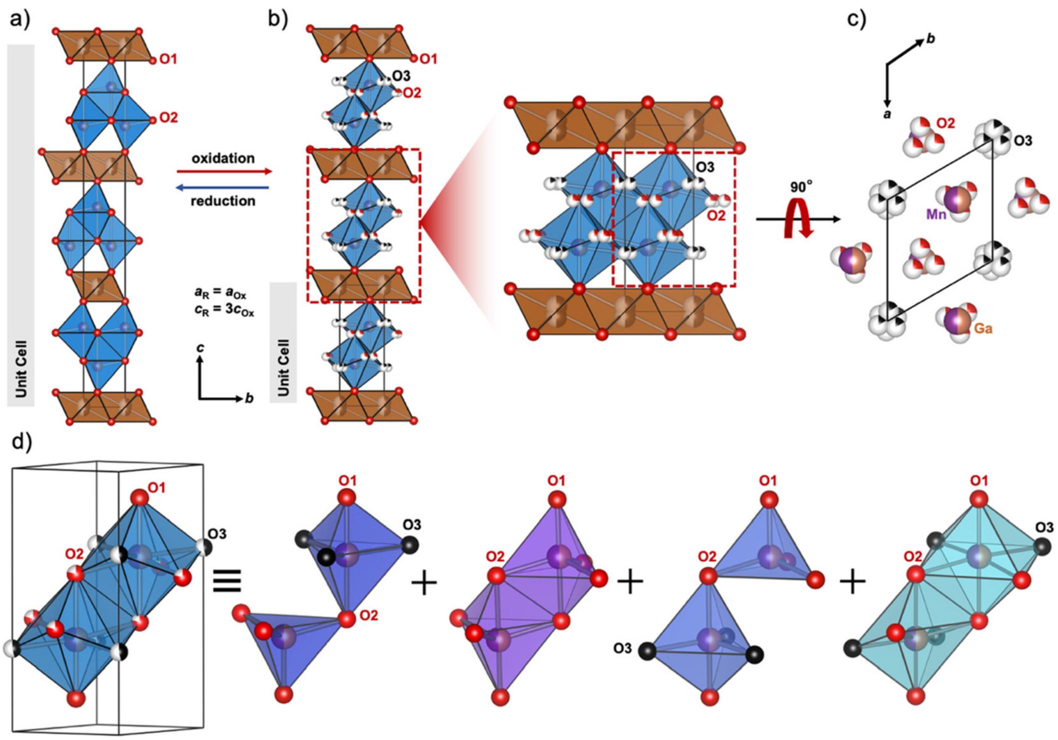

Fig. 3 Crystal structures of (a) $LuMnGaO_4$ ($R\bar{3}m$) and (b) $LuMnGaO_{4.5}$ ($P\bar{3}$) along the *c*-axis. (c) $LuMnGaO_4$ structure rotated 90° to display the ab plane, highlighting the disordered oxygen. (d) Superimposed Mn/Ga–O_n polyhedra (n = 4, 5, 6) forming the average Mn/Ga–O_n double layer structure.

Table 1 Structural parameters obtained from Rietveld refinement of neutron diffraction data for $LuMnGaO_4$ ($R\bar{3}m$) at 300 K, with R_{wp} = 4.851%

Atom	Wyc. pos.	x	y	z	Site occ.	U_{iso}	U_{11}	U_{22}	U_{33}	U_{12}	U_{13}	U_{23}
Lu	6c	0	0	0.00675(4)	0.5	0.0047(2)						
Mn	6c	0	0	0.22046(6)	0.5	0.0045(3)						
Ga	6c	0	0	0.22046(6)	0.5	0.0045(3)						
O1	6c	0	0	0.29271(3)	1		0.0267(4)	0.0267(4)	0.0363(5)	0.0134(2)	0	0
O2	6c	0	0	0.29271(3)	1		0.0267(4)	0.0267(4)	0.0363(5)	0.0134(2)	0	0

Lattice parameters. $a = b = 3.42515(2)$ Å, $c = 25.7621(2)$ Å, $\alpha = \beta = 90°$, $\gamma = 120°$, vol. = 261.741(2) $Å^3$.

Table 2 Structural parameters obtained from Rietveld refinement of neutron diffraction data for $LuMnGaO_{4.5}$ ($P\bar{3}$) at 300 K, with R_{wp} = 6.196 %

Atom	Wyc. pos.	x	y	z	Site occ.	U_{iso}
Lu	2c	0	0	0.0284(4)	0.5	0.0148(6)
Mn	2d	0.66667	0.33333	0.345(1)	0.5	0.019(2)
Ga	2d	0.66667	0.33333	0.345(1)	0.5	0.019(2)
O1	2d	0.66667	0.33333	0.1227(3)	1	0.0203(4)
O2	6g	0.242(2)	0.552(1)	0.4061(4)	0.265(2)	0.011(1)
O3	6g	0.011(4)	0.087(2)	0.3147(5)	0.152(2)	0.002(2)

Lattice parameters. $a = b = 3.4801(1)$ Å, $c = 8.1714(2)$ Å, $\alpha = \beta = 90°$, $\gamma = 120°$, vol. = 85.707(3) $Å^3$.

3.4 Diffuse scattering and modulation structures

Fig. 4a, c and d, f present the SAED patterns for the reduced and oxidized phases, respectively, with the reciprocal lattice indicated and several reflections (h, k, l) labeled. In the reduced phase, the SAED pattern along the [001] zone axis in Fig. 4a reveals regular Bragg spots of {110} and {300}. Additionally, weak {100} Bragg reflections are present, which might result from multiple scattering due to the increased specimen thickness. The electron diffraction was performed on crushed powders with a selected-area aperture covering a dimension of a few hundred nm scale. Furthermore, the SAED pattern along the [110] zone axis in

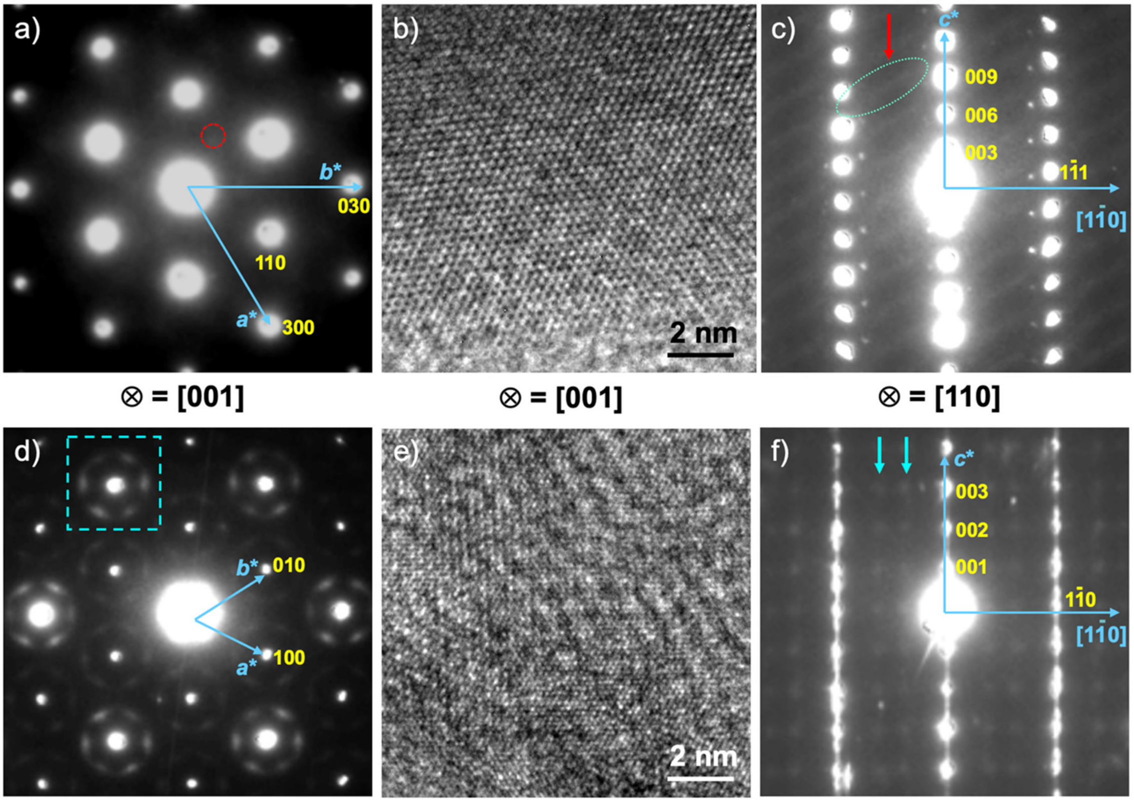

Fig. 4 Selected-area electron diffraction patterns along [001] (a and d) and [110] (c and f) zones axis for (a and c) LuMnGaO$_4$ and (d and f) LuMnGaO$_{4.5}$. Indexed diffraction spots are labeled in yellow. In (a and c), diffuse scattering is indicated by red circles and streaks marked by green circle observed in LuMnGaO$_4$. In (d and f), the blue cube and arrows indicate structural modulation in LuMnGaO$_{4.5}$. (b and e) The HRTEM images recorded along the [001] zone axis for (b) LuMnGaO$_4$ and (e) LuMnGaO$_{4.5}$. It reveals modulation structure in (e).

Fig. 4c reveals regular Bragg spots accompanied by weak diffuse streaks, which are within the green circle indicated by the red arrow. This diffuse streak is parallel to the [106] direction and may correspond to the background hump observed in the neutron diffraction pattern at lower Q (Fig. 2a).

Upon oxidation and structural transformation, the SAED patterns show significant differences. First, the [001] zone axis SAED pattern for LuMnGaO$_{4.5}$ in Fig. 4d reveals a sharp intensity of the {100} Bragg spots compared to the weak reflection condition in Fig. 4a, indicating different reflection conditions. Second, six additional diffuse satellite reflections appear around each Bragg reflection, marked by a blue cube, which cannot be indexed using the unit cell of the $P\bar{3}$ space group listed in Table 2. Furthermore, the [110] zone axis SAED pattern for LuMnGaO$_{4.5}$ in Fig. 4f reveals additional weaker {1/3 0 0} and {0 2/3 0} superlattice reflections, in contrast to the diffuse streaks seen in Fig. 4c. These satellite reflections indicate the presence of structural modulations, which lead to a new periodic arrangement in the HRTEM images from Fig. 4b to d, caused by oxygen order leading to a superlattice. These satellite peaks are also evident in the SXPD data shown in Fig. 5.

3.5 Structural evolution of LuMnGaO$_4$ during oxygen insertion

An *in situ* SXPD experiment was conducted to investigate the structural evolution of LuMnGaO$_4$ upon heating. Fig. 5a shows the contour plots of *in situ* SXPD patterns for LuMnGaO$_4$ heated in air up to 700 °C. Below 350 °C, no new reflections were observed, indicating that the room temperature structure of LuMnGaO$_4$ was maintained. A phase transition began at approximately 350 °C, consistent with the TGA results (Fig. 1a). Sequential refinement of the *in situ* measurements revealed that this transition differs from that of the parent phase LuFe$_2$O$_4$, which forms a supercell structure around 250 °C, as evidenced by satellite reflections in SXPD data.[19] Additionally, an intermediate phase appears before LuFe$_2$O$_4$ fully oxidizes to LuFe$_2$O$_{4.5}$. In contrast, for LuMnGaO$_4$ the phase transition occurs without an intermediate phase and directly coincides with oxygen absorption.

Fig. 5c presents four selected SXPD patterns from the sequential *in situ* measurements at 50 °C, 350 °C, 450 °C, and 600 °C, illustrating the changes in SXPD patterns upon heating. The evolution of lattice parameters a and c over the entire temperature range is depicted in Fig. 6, where the c parameters of the oxidized phases ($P\bar{3}$) are multiplied by three for direct comparison with those of the reduced phases ($R\bar{3}m$). As the reduced phase oxidizes, the lattice parameter a increases, while c decreases. These structural changes align well with the weight changes observed in TGA. The Rietveld refinements of the SXPD patterns at 50 °C, 350 °C, 450 °C, and 600 °C are shown in Fig. S13–S16.† A closer examination of the

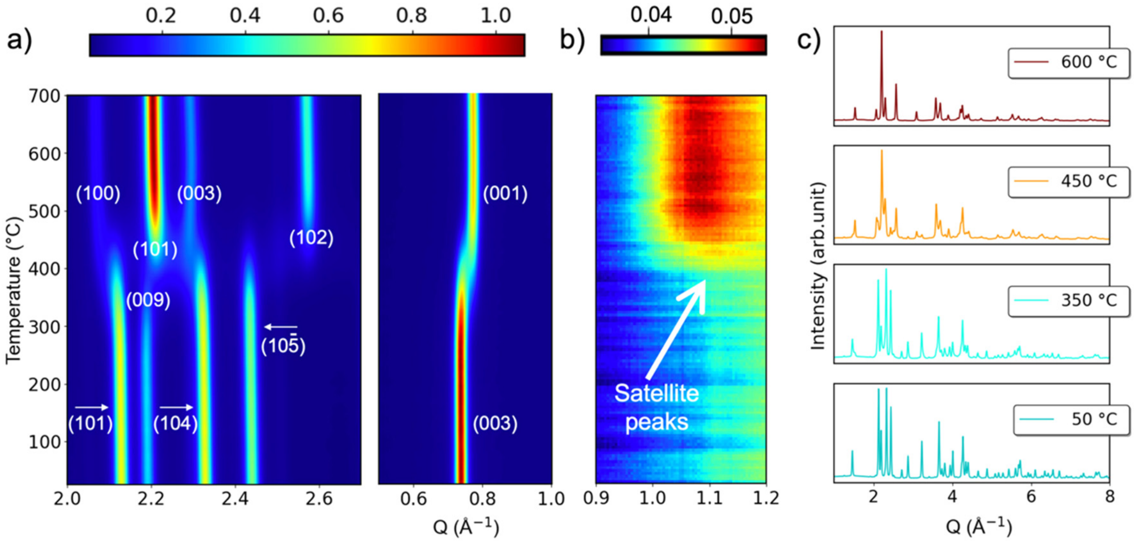

Fig. 5 *In situ* SXPD of $LuMnGaO_4$ as it oxidizes. (a) Contour plots of *in situ* SXPD data for $LuMnGaO_4$ heated in air from 25 °C to 700 °C. (b) Enlarged view (magnified 20×) highlighting the appearance of satellite peaks. (c) Selected diffraction patterns at 50 °C, 350 °C, 450 °C, and 600 °C.

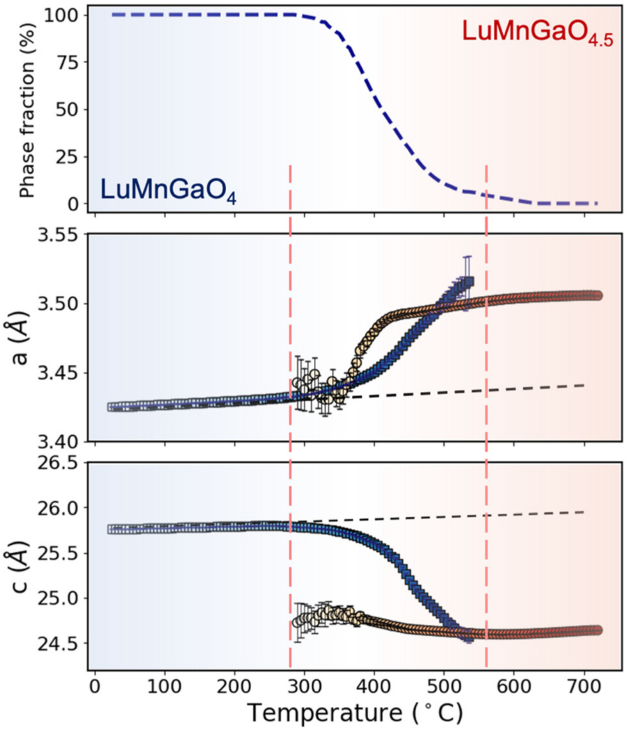

Fig. 6 Evolution of phase fractions and lattice parameters, *a* and normalized *c*, as a function of temperature in air, derived from sequential Rietveld refinements of *in situ* SXPD data. The top panel shows the phase fraction transition from $LuMnGaO_4$ to $LuMnGaO_{4.5}$, while the middle and bottom panels display the corresponding changes in the lattice parameters *a* and *c*, respectively. The red dashed lines indicate where phase transformation or structural changes occur.

magnified SXPD patterns reveals additional satellite peaks (Fig. 5b and Fig. S18†), also observed in the SAED patterns (Fig. 4c and d). These peaks emerge above 400 °C during heating and indicate a structural modulation that resembles one observed previously in $LnMnFeO_4$.[21]

3.6 Color change from $LuMnGaO_4$ to $LuMnGaO_{4.5}$

The structures of $LuMnGaO_4$ and related compounds are closely correlated with the $YIn_{1-x}Mn_xO_3$ phases, as studied by Subramanian, *et al.*, where the hexagonal structure consists of layers of Y^{3+} ions separating layers of corner-shared MO_5 trigonal bipyramids (M = In, Mn).[44–46] This compound exhibits a bright-blue hue due to the crystal field splitting of Mn^{3+} in trigonal bipyramidal coordination. Building on this understanding, we investigated the distinct color change in $LuMnGaO_4$ upon oxygen insertion, focusing on the role of the Mn site during oxidation.

The reduced phase of $LuMnGaO_4$ exhibits a greenish-grey hue as shown in Fig. 7. Following oxidation, the color transitions to black. Diffuse reflectance spectra and approximated absorbance spectra, calculated using the Kubelka–Munk function, confirmed this chromatic shift.[47] The blue curve in Fig. 7 represents the absorbance spectra of $LuMnGaO_4$, with two major peaks at 3.7 eV and 2 eV, while the red curve for $LuMnGaO_{4.5}$ displays broad absorption across the visible spectrum, consistent with the black color. The absorbance spectrum of the impurity, $Lu_3Ga_5O_{12}$, is included in Fig. S8,† which corresponds to the white color of the material.

The color change could be attributed to either a d–d transition or ligand-to-metal charge transfer. First, we describe the transition arising from the Mn/Ga–O trigonal bipyramidal coordination. Subramanian *et al.* explained that the blue hue of $Y(In,Mn)O_3$ arises from the crystal field splitting of Mn^{3+} in trigonal bipyramid coordination.[45] Similarly, $LuMnGaO_4$ consists of double layers of edge-sharing trigonal bipyramidal units, where Mn and Ga are disordered at the same site. In the reduced phase, Mn^{2+}, with five d-electrons, occupies the

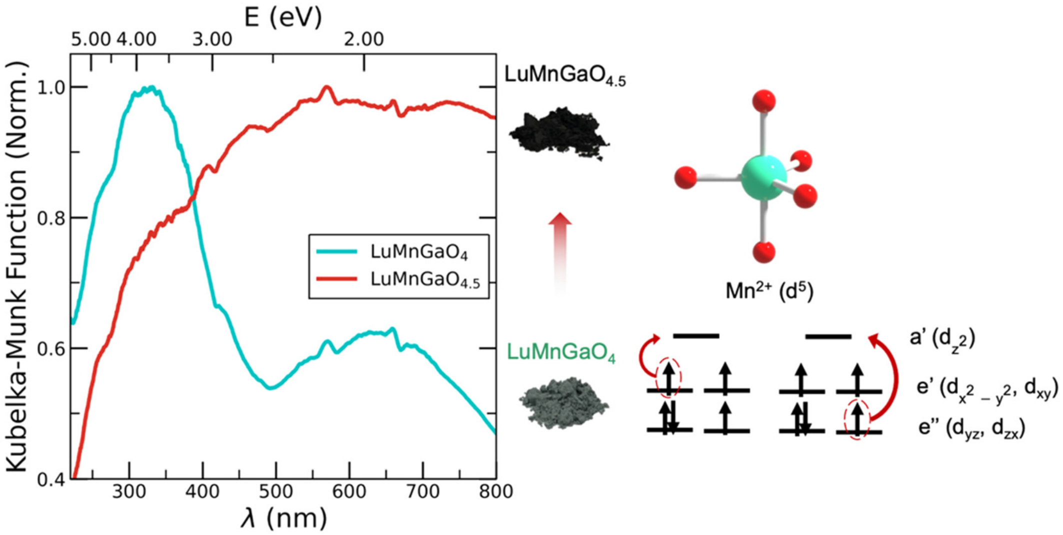

Fig. 7 Color change from $LuMnGaO_4$ to $LuMnGaO_{4.5}$, and corresponding UV-vis spectroscopy measurements. The *y*-axis represents the Kubelka–Munk transformed absorbance spectra. The schematic energy levels for Mn^{2+} 3d orbitals in trigonal bipyramidal coordination are shown, with possible electronic transitions (e′ → a′ and e″ → a′) contributing to the observed color of $LuMnGaO_4$.

doubly degenerate e′ and e″ energy levels. Spin- and symmetry-allowed transitions would therefore include e′ → a′ and e″ → a′, corresponding to the absorption peaks at 2 eV and 3.7 eV, respectively. The lack of absorption in the 450–600 nm range results in the greenish-grey hue. Upon oxidation, Mn oxidizes to the +3 state, as confirmed by XPS and EPR spectra (Fig. 1b and c). This oxidation alters the coordination geometry from trigonal bipyramidal to a combination of octahedral, tetrahedral, and trigonal bipyramidal configurations. These complex crystal field environments produce broad absorption across the visible spectrum, which results in the black color.

The second possibility to understand the origin of color in $LuMnGaO_4$ is the ligand-to-metal charge transfer (LMCT). Manganese(ii) oxide (MnO), which crystallizes in a cubic rock-salt structure with Mn^{2+} ions in octahedral coordination, exhibits a green color.[48] MnO has been widely studied as a borderline between a Mott insulator and a charge-transfer insulator.[49,50] The optical band gaps of the colloidal MnO nanoparticles have been reported to be 3.19 eV and 2.18 eV, attributed to the direct and indirect transitions respectively, arising from the O 2p–Mn e_g transitions.[51] Although the Mn/Ga sites in $LuMnGaO_4$ adopt a trigonal bipyramidal coordination rather than an octahedral, the UV-vis absorption occurred at 3.7 eV and 2 eV are similar to those in MnO. The resemblance suggests that LMCT transitions involving O 2p to Mn 3d orbitals may also contribute to the optical absorption in $LuMnGaO_4$ alongside crystal field effects.

The pronounced color change from greenish-grey ($LuMnGaO_4$) to black ($LuMnGaO_{4.5}$) highlights the potential of this material for colorimetric oxygen sensing. Color sensing, which translates color changes into quantifiable data, has applications in environmental monitoring, diagnostics, and industrial processes.[52,53] These systems leverage reflected or transmitted light to detect chromatic transitions, employing advanced algorithms and optical systems for enhanced sensitivity.[54] In $LuMnGaO_4$, the oxidation-induced Mn coordination transformation enables efficient oxygen detection, positioning this material as a potential candidate for oxygen and colorimetric sensing applications.

4. Conclusion

In this study, we have synthesized and characterized the reduced and oxidized phases of $LuMnGaO_4$, exploring their structural evolution and unique color changes upon oxygen insertion. Using neutron and SXPD diffraction, we determined that the reduced phase ($LuMnGaO_4$) crystallizes in the $R\bar{3}m$ space group, while the oxidized phase ($LuMnGaO_{4.5}$) adopts the $P\bar{3}$ space group. Our *in situ* SXPD experiments revealed a phase transition during oxidation, accompanied by a distinct shift in color from greenish-grey to black, confirmed through UV-visible spectroscopy. The observed color change is attributed to changes in the coordination geometry of the Mn/Ga–O layer, which transitions from trigonal bipyramid to a combination of octahedral, tetrahedral, and trigonal bipyramidal configurations. The structural modulations and satellite peaks indicate complex oxygen ordering and disordering. These findings highlight the potential of $LuMnGaO_4$ as a bifunctional material, with promising applications in both oxygen transport and sensing technologies at relatively low temperatures. This study provides new insight into the structure–property relationships of AB_2O_4-type compounds and lays the groundwork for further investigations into the effects of elemental substitution and phase transitions in oxygen carrier materials.

Conflicts of interest

There are no conflicts of interest to declare.

Data availability

The data supporting this article have been included as part of the ESI.†

Acknowledgements

We acknowledge support from the NIST Cooperative Agreement No. 70NANB20H139 and 70NANB17H301 for support. Use of the Spallation Neutron Source (POWGEN experiment IPTS-30479) at Oak Ridge National Laboratory and the Advanced Photon Source at Argonne National Laboratory was supported by the U.S. Department of Energy, Office of Science, Office of Basic Energy Sciences, under Contract No. DE-AC02-06CH11357. We thank Mr Kevin Beyer at 11-IDC, APS, for his assistance with the *in situ* X-ray diffraction experiment. We also thank Dr Karen Gaskell for insightful discussions on the XPS analysis. Part of this research was carried out using the shared facilities of the Materials Research Science and Engineering Center (MRSEC) under NSF Award No. DMR-2308708.

References

1 J. W. Lekse, S. Natesakhawat, D. Alfonso and C. Matranga, An experimental and computational investigation of the oxygen storage properties of $BaLnFe_2O_{5+\delta}$ and $BaLnCo_2O_{5+\delta}$ (Ln = La, Y) perovskites, *J. Mater. Chem. A*, 2014, **2**, 2397–2404.

2 J. E. Readman, A. Olafsen, Y. Larring and R. Blom, $La_{0.8}Sr_{0.2}Co_{0.2}Fe_{0.8}O_{3-\delta}$ as a potential oxygen carrier in a chemical looping type reactor, an *in situ* powder X-ray diffraction study, *J. Mater. Chem.*, 2005, **15**, 1931–1937.

3 A. Klimkowicz, K. Świerczek, A. Takasaki and B. Dabrowski, Oxygen storage capability in Co- and Fe-containing perovskite-type oxides, *Solid State Ionics*, 2014, **257**, 23–28.

4 Z. Yang, Y. S. Lin and Y. Zeng, High-Temperature Sorption Process for Air Separation and Oxygen Removal, *Ind. Eng. Chem. Res.*, 2002, **41**, 2775–2784.

5 M. Karppinen, H. Yamauchi, S. Otani, T. Fujita, T. Motohashi, Y.-H. Huang, M. Valkeapää and H. Fjellvåg, Oxygen Nonstoichiometry in $YBaCo_4O_{7+\delta}$: Large Low-Temperature Oxygen Absorption/Desorption Capability, *Chem. Mater.*, 2006, **18**, 490–494.

6 S. Abanades, A Review of Oxygen Carrier Materials and Related Thermochemical Redox Processes for Concentrating Solar Thermal Applications, *Materials*, 2023, **16**, 3582.

7 M. Rydén, A. Lyngfelt, T. Mattisson, D. Chen, A. Holmen and E. Bjørgum, Novel oxygen-carrier materials for chemical-looping combustion and chemical-looping reforming; $La_xSr_{1-x}Fe_yCo_{1-y}O_{3-\delta}$ perovskites and mixed-metal oxides of NiO, Fe_2O_3 and Mn_3O_4, *Int. J. Greenhouse Gas Control*, 2008, **2**, 21–36.

8 W. C. Chueh, C. Falter, M. Abbott, D. Scipio, P. Furler, S. M. Haile and A. Steinfeld, High-Flux Solar-Driven Thermochemical Dissociation of CO_2 and H_2O Using Nonstoichiometric Ceria, *Science*, 2010, **330**, 1797–1801.

9 M. Ezbiri, M. Takacs, D. Theiler, R. Michalsky and A. Steinfeld, Tunable thermodynamic activity of $La_xSr_{1-x}Mn_yAl_{1-y}O_{3-\delta}$ ($0 \leq x \leq 1$, $0 \leq y \leq 1$) perovskites for solar thermochemical fuel synthesis, *J. Mater. Chem. A*, 2017, **5**, 4172–4182.

10 D. R. Barcellos, M. D. Sanders, J. Tong, A. H. McDaniel and R. P. O'Hayre, $BaCe_{0.25}Mn_{0.75}$ $O_{3-\delta}$ —a promising perovskite-type oxide for solar thermochemical hydrogen production, *Energy Environ. Sci.*, 2018, **11**, 3256–3265.

11 N. Kimizuka, A. Takenaka, Y. Sasada and T. Katsura, A series of new compounds $A^{3+}Fe_2O_4$ (A = Ho, Er, Tm, Yb, and Lu), *Solid State Commun.*, 1974, **15**, 1321–1323.

12 N. Kimizuka and E. Takayama, $Ln(Fe^{3+}M^{2+})O_4$ compounds with layer structure [Ln : Y, Er, Tm, Yb, and Lu, M : Mg, Mn, Co, Cu, and Zn], *J. Solid State Chem.*, 1981, **40**, 109–116.

13 N. Kimizuka and E. Takayama, $Ln(GaM^{2+})O_4$ and $Ln(AlMn^{2+})O_4$ compounds having a layer structure [*Ln* = Lu, Yb, Tm, Er, Ho, and Y, and *M* = Mg, Mn, Co, Cu, and Zn], *J. Solid State Chem.*, 1982, **41**, 166–173.

14 N. Kimizuka and T. Mohri, Structural classification of $RAO_3(MO)_n$ compounds (*R* = Sc, In, Y, or lanthanides; *A* = Fe(III), Ga, Cr, or Al; *M* = divalent cation; n = 1–11), *J. Solid State Chem.*, 1989, **78**, 98–107.

15 N. Kimizuka and E. Takayama, , Survey of the phase formation in the Yb_2O_3–Ga_2O_3–MO and Yb_2O_3–Cr_2O_3–*M*O systems in air at high temperatures (*M*: Co, Ni, Cu, and Zn), *J. Solid State Chem.*, 1982, **43**, 278–284.

16 M. Hervieu, A. Guesdon, J. Bourgeois, E. Elkaïm, M. Poienar, F. Damay, J. Rouquette, A. Maignan and C. Martin, Oxygen storage capacity and structural flexibility of $LuFe_2O_{4+x}$ ($0 \leq x \leq 0.5$), *Nat. Mater.*, 2014, **13**, 74–80.

17 M. Hervieu, F. Damay, A. Maignan and C. Martin, Rare earth ferrites $LuFe_2O_{4\pm x}$ polymorphism, polytypism and metastable phases, *Solid State Sci.*, 2015, **48**, A1–A16.

18 T. Li, R. Jayathilake, L. Balisetty, Y. Zhang, B. Wilfong, T. J. Diethrich and E. E. Rodriguez, Crystal field-induced lattice expansion upon reversible oxygen uptake/release in $YbMn_xFe_{2-x}O_4$, *Mater. Adv.*, 2021, **3**, 1087–1100.

19 R. S. Jayathilake, B. D. Levitas and E. E. Rodriguez, *In situ* diffraction studies on reversible oxygen uptake and release in $AFe_2O_{4+\delta}$ (A = Lu, Yb, Y, and In), *J. Mater. Chem. A*, 2018, **6**, 4801–4810.

20 S. Nicoud, M. Huvé, O. Hernandez, A. Pautrat, M. Duttine, A. Wattiaux, C. Colin, H. Kabbour and O. Mentré, Comprehensive Study of Oxygen Storage in $YbFe_2O_{4+x}$ ($x \leq 0.5$): Unprecedented Coexistence of FeO_n Polyhedra in One Single Phase, *J. Am. Chem. Soc.*, 2017, **139**, 17031–17043.

21 T. Li, S.-C. Liou, S. J. Hong, Q. Zhang, H. C. Mandujano and E. E. Rodriguez, Structural modulation and spin glassiness upon oxidation in oxygen storage material *Ln*FeMnO$_{4+x}$ for *Ln* = Y, Lu, and Yb, *APL Mater.*, 2023, **11**, 061120.

22 R. Ramamoorthy, P. K. Dutta and S. A. Akbar, Oxygen sensors: Materials, methods, designs and applications, *J. Mater. Sci.*, 2003, **38**, 4271–4282.

23 X. Meng, S. Kim, P. Puligundla and S. Ko, Carbon dioxide and oxygen gas sensors-possible application for monitoring quality, freshness, and safety of agricultural and food products with emphasis on importance of analytical signals and their transformation, *J. Korean Soc. Appl. Biol. Chem.*, 2014, **57**, 723–733.

24 A. W. Hempel, D. B. Papkovsky and J. P. Kerry, Use of Optical Oxygen Sensors in Non-Destructively Determining the Levels of Oxygen Present in Combined Vacuum and Modified Atmosphere Packaged Pre-Cooked Convenience-Style Foods and the Use of Ethanol Emitters to Extend Product Shelf-Life, *Foods*, 2013, **2**, 507–520.

25 X. Wang and O. S. Wolfbeis, Optical methods for sensing and imaging oxygen: materials, spectroscopies and applications, *Chem. Soc. Rev.*, 2014, **43**, 3666–3761.

26 J. W. Schwank and M. DiBattista, Oxygen Sensors: Materials and Applications, *MRS Bull.*, 1999, **24**, 44–48.

27 W. Bulowski, R. Knura, R. P. Socha, M. Basiura, K. Skibińska and M. Wojnicki, Thin Film Semiconductor Metal Oxide Oxygen Sensors: Limitations, Challenges, and Future Progress, *Electronics*, 2024, **13**, 3409.

28 N. Fairley, V. Fernandez, M. Richard-Plouet, C. Guillot-Deudon, J. Walton, E. Smith, D. Flahaut, M. Greiner, M. Biesinger, S. Tougaard, D. Morgan and J. Baltrusaitis, Systematic and collaborative approach to problem solving using X-ray photoelectron spectroscopy, *Appl. Surf. Sci. Adv.*, 2021, **5**, 100112.

29 S. Stoll and A. Schweiger, EasySpin, a comprehensive software package for spectral simulation and analysis in EPR, *J. Magn. Reson.*, 2006, **178**, 42–55.

30 A. Huq, M. Kirkham, P. F. Peterson, J. P. Hodges, P. S. Whitfield, K. Page, T. Hűgle, E. B. Iverson, A. Parizzi and G. Rennich, POWGEN: rebuild of a third-generation powder diffractometer at the Spallation Neutron Source, *J. Appl. Crystallogr.*, 2019, **52**, 1189–1201.

31 B. H. Toby and R. B. V. Dreele, GSAS–II: the genesis of a modern open–source all purpose crystallography software package, *J. Appl. Crystallogr.*, 2013, **46**, 544–549.

32 V. D. Castro and G. Polzonetti, XPS study of MnO oxidation, *J. Electron Spectrosc. Relat. Phenom.*, 1989, **48**, 117–123.

33 H. W. Nesbitt and D. Banerjee, Interpretation of XPS Mn(2p) spectra of Mn oxyhydroxides and constraints on the mechanism of MnO$_2$ precipitation, *Am. Mineral.*, 1998, **83**, 305–315.

34 E. S. Ilton, J. E. Post, P. J. Heaney, F. T. Ling and S. N. Kerisit, XPS determination of Mn oxidation states in Mn (hydr)oxides, *Appl. Surf. Sci.*, 2016, **366**, 475–485.

35 J. M. Cerrato, M. F. Hochella, W. R. Knocke, A. M. Dietrich and T. F. Cromer, Use of XPS to Identify the Oxidation State of Mn in Solid Surfaces of Filtration Media Oxide Samples from Drinking Water Treatment Plants, *Environ. Sci. Technol.*, 2010, **44**, 5881–5886.

36 A. Abragam and B. Bleaney, *Electron Paramagnetic Resonance of Tranition Ion*, Dover Publications, 2012.

37 R. Grajczyk and M. A. Subramanian, Structure–property relationships of YbFe$_2$O$_4$– and Yb$_2$Fe$_3$O$_7$–type layered oxides: A bird's eye view, *Prog. Solid State Chem.*, 2015, **43**, 37–46.

38 J. Ilda, M. Tanaka and Y. Nakagawa, Magnetization of Single Crystal YFeMnO$_4$, *J. Phys. Soc. Jpn.*, 1990, **59**, 4443–4448.

39 M. Isobe, M. Nespolo, J. Iida and N. Kimizuka, Crystal structure and charge distribution of YbFeMnO$_4$, *Acta Crystallogr., Sect. B*, 2000, **56**, 805–810.

40 R. J. Cava, A. P. Ramirez, Q. Huang and J. J. Krajewski, Compounds with the YbFe$_2$O$_4$ Structure Type: Frustrated Magnetism and Spin-Glass Behavior, *J. Solid State Chem.*, 1998, **140**, 337–344.

41 R. D. Shannon, Revised Effective Ionic Radii and Systematic Studies of Interatomic Distances in Halides and Chalcogenides, *Acta Crystallogr., Sect. A*, 1976, 751–767.

42 J. Bourgeois, M. Hervieu, M. Poienar, A. M. Abakumov, E. Elkaïm, M. T. Sougrati, F. Porcher, F. Damay, J. Rouquette, G. V. Tendeloo, A. Maignan, J. Haines and C. Martin, Evidence of oxygen-dependent modulation in LuFe$_2$O$_4$, *Phys. Rev. B*, 2012, **85**, 064102.

43 S. Deng, L. Wu, H. Cheng, J.-C. Zheng, S. Cheng, J. Li, W. Wang, J. Shen, J. Tao, J. Zhu and Y. Zhu, Charge-Lattice Coupling in Hole-Doped LuFe$_2$O$_{4+\delta}$: The Origin of Second-Order Modulation, *Phys. Rev. Lett.*, 2019, **122**, 126401.

44 A. E. Smith, H. Mizoguchi, K. Delaney, N. A. Spaldin, A. W. Sleight and M. A. Subramanian, Mn^{3+} in Trigonal Bipyramidal Coordination: A New Blue Chromophore, *J. Am. Chem. Soc.*, 2009, **131**, 17084–17086.

45 J. Li and M. A. Subramanian, Inorganic pigments with transition metal chromophores at trigonal bipyramidal coordination: Y(In,Mn)O$_3$ blues and beyond, *J. Solid State Chem.*, 2019, **272**, 9–20.

46 A. E. Smith, M. C. Comstock and M. A. Subramanian, Spectral properties of the UV absorbing and near-IR reflecting blue pigment, YIn$_{1(-x}$Mn$_x$O$_3$, *Dyes Pigm.*, 2016, **133**, 214–221.

47 P. Kubelka and F. Munk, Ein Beitrag zur Optik der Farbanstriche, *Z. Techn. Phys.*, 1931, **12**, 593–601.

48 G. R. Levi, The crystal structure of MnO, *Rend. Ist. Lomb. Sci. Lett., Cl. Sci. Mat. Nat.*, 1924, **57**, 619–624.

49 J. Liu, T. Yang, A. Xu, R. L. Martin, Y. Yang, H. Jiao, Y. Li and X.-D. Wen, Predication of screened hybrid functional on transition metal monoxides: From Mott insulator to charge transfer insulator, *J. Alloys Compd.*, 2019, **808**, 151707.

50 A. Fujimori, N. Kimizuka, T. Akahane, T. Chiba, S. Kimura, F. Minami, K. Siratori, M. Taniguchi, S. Ogawa and S. Suga, Electronic structure of MnO, *Phys. Rev. B*, 1990, **42**, 7580–7586.

51 B. K. Pandey, A. K. Shahi and R. Gopal, Optical and Electrical Transport Properties of MnO Nanoparticles, *Mater. Focus*, 2013, **2**, 221–226.

52 B. Liu, J. Zhuang and G. Wei, Recent advances in the design of colorimetric sensors for environmental monitoring, *Environ. Sci.: Nano*, 2020, **7**, 2195–2213.

53 R. Umapathi, S. Sonwal, M. J. Lee, G. M. Rani, E.-S. Lee, T.-J. Jeon, S.-M. Kang, M.-H. Oh and Y. S. Huh, Colorimetric based on-site sensing strategies for the rapid detection of pesticides in agricultural foods: New horizons, perspectives, and challenges, *Coord. Chem. Rev.*, 2021, **446**, 214061.

54 Z. Jin, W. Yim, M. Retout, E. Housel, W. Zhong, J. Zhou, M. S. Strano and J. V. Jokerst, Colorimetric sensing for translational applications: from colorants to mechanisms, *Chem. Soc. Rev.*, 2024, **53**, 7681–7741.